Biomaterials

CrossMark

Polyamido amine (PAMAM)-grafted magnetic nanotubes as emerging platforms for the delivery and sustained release of silibinin

Gloria Chávez[1], Cristian H. Campos[1], Verónica A. Jiménez[2], Cecilia C. Torres[2], Carola Díaz[1], Gorka Salas[3], Leonardo Guzmán[4], and Joel B. Alderete[1,*]

[1] *Facultad de Ciencias Químicas, Universidad de Concepción, Edmundo Larenas 129, Concepción, Chile*

[2] *Departamento de Ciencias Químicas, Facultad de Ciencias Exactas, Universidad Andres Bello, Sede Concepción, Autopista Concepción-Talcahuano, 7100 Talcahuano, Chile*

[3] *iMdea-Nanociencia, Campus Universitario de Cantoblanco, 28049 Madrid, Spain*

[4] *Departamento de Fisiología, Facultad de Ciencias Biológicas, Universidad de Concepción, 403901 Concepción, Chile*

ABSTRACT

This work reports the synthesis of surface-modified iron oxide magnetic nanotubes (Fe$_3$O$_4$NT) with poly(amido amine) dendrimers of the third generation (PAMAM-G3) as novel nanomaterials for potential drug-delivery applications. Fe$_3$O$_4$NT were obtained by reduction of α-Fe$_2$O$_3$ nanotubes, which were synthesized following a hydrothermal strategy using SO$_4$$^{2-}$/H$_2PO_4$$^-$ to control the size and morphology of the prepared materials. Fe$_3$O$_4$NT were further functionalized with PAMAM-G3 moieties using a silane coupling agent. Pristine and PAMAM-modified Fe$_3$O$_4$NT were characterized through TEM, FTIR, XRD, N$_2$ adsorption–desorption isotherms and VSM measurements, which confirmed the nanotubular morphology and magnetic behavior for both systems, and TGA analyses, which revealed a PAMAM grafting percentage of 16.8%. The effect of PAMAM conjugation on the adsorption and release properties of Fe$_3$O$_4$NT was examined using silibinin as model poorly soluble drug compound. Our results revealed that PAMAM grafting increased the maximum amount of adsorbed drug from 675 mg g^{-1} in pristine Fe$_3$O$_4$NT to 825 mg g^{-1} in PAMAM-Fe$_3$O$_4$NT. These quantities exceed by far the drug-loading capacity of other pristine and PAMAM-modified nanotubular systems, which constitutes a relevant outcome for the present study.

Introduction

In the last decades, nanoscience and nanotechnology have played a leading role in the development of diverse research fields such as electronics, catalysis, biocatalysis and biomedicine. In this context, nanomaterials with different shape and topology have been extensively studied as vehicles for drug encapsulation and sustained release of a wide variety of therapeutic agents, ranging from small drugs to

🍃 Springer

proteins [1–4]. Within diversely shaped materials, nanotubular structures present advantageous features for drug encapsulation and delivery compared to conventional spherical counterparts due to their enhanced drug-loading capacity and distinctive inner and outer surfaces, which allow the incorporation of functional moieties to modulate their properties [5–9].

Within biomedical nanomaterials, magnetic nanostructures have emerged as valuable platforms for the design of image contrast agents, drug carriers and controlled drug-delivery systems. Particularly, iron oxide magnetic nanoparticles of different size and morphology are being assayed as promising nanomaterials for drug-delivery applications, and many efforts have been made in the synthesis of iron oxide magnetic nanostructures with well-defined morphologies, such as nanocrystals, polyhedra, cubes, rods and tubes [10, 11]. Regarding to this subject, hydrothermal synthesis has proven to be a simple successful experimental strategy to obtain functional nanostructures with tunable shapes and high reproducibility [12, 13]. Using a hydrothermal route and a subsequent H_2 reduction treatment, Jia et al. reported a simple procedure to produce magnetic Fe_3O_4 nanotubes (Fe_3O_4NT), starting from $FeCl_3 \cdot 6H_2O$ as iron source and Na_2SO_4 and $NH_4H_2PO_4$ as morphology controllers, opening the possibility of creating a range of three-dimensional structures by varying the $SO_4^{2-}/H_2PO_4^{-}$ ratio during the hydrothermal synthesis [14–16].

In the past years, Fe_3O_4NT have shown remarkable properties for the encapsulation and controlled release of drugs, oligomers and macromolecules, which can be safely transported into the cell avoiding hydrolytic degradation or insolubility behavior during their delivery at the specific target site [17]. Despite these promising features, the clinical application of Fe_3O_4NT is largely limited by their colloidal aggregation, which can be overcome through the surface modification of these materials with diverse polymeric or proteic moieties [17–21]. The surface modification of Fe_3O_4NT has also proven to be a successful strategy to increase the drug-loading capacity, stability and biocompatibility of these nanomaterials, which encourages the search for novel possibilities to improve the performance of Fe_3O_4NT based on the covalent attachment of polymeric systems with intrinsic drug-encapsulating properties, such as poly(amido amine) (PAMAM) dendrimers. In

the past years, several studies have explored the synthesis of hybrid materials combining iron oxide nanoparticles with PAMAM dendrimers with a diversity of purposes [22–25]. Nevertheless, to the best of our knowledge, the use of PAMAM dendrimers as surface modifiers of magnetic Fe_3O_4NT has not been reported in the literature and constitutes a challenging task for the design of novel nanomaterials for drug-delivery applications. In very recent reports we demonstrated that the surface covalent attachment of PAMAM dendrimers improved the drug-loading and release properties of Al_2O_3 and TiO_2 nanotubes [26, 27], which is an auspicious result to explore the use of these polymeric moieties as surface modifiers for magnetic Fe_3O_4NT, as reported in the present work.

PAMAM dendrimers are monodisperse synthetic polymers constituted by a central core of ethylene diamine, branches of amido amine moieties and terminal surface amino groups. Because of its unique architecture, PAMAM dendrimers have been vastly studied as drug-delivery systems due to their capability to complex small-size molecules and enhance the solubility and bioavailability of hydrophobic and sparingly soluble drugs [28, 29]. A major limitation of PAMAM dendrimers in drug-delivery applications arises from the reported cytotoxicity of high-generation species [30, 31], which can be overcome by using low-generation dendrimers since they are non-immunogenic and exhibit minimal cytotoxicity [32, 33]. Based on the previous background, this work describes the synthesis of surface-modified magnetic Fe_3O_4NT with PAMAM dendrimers of the third generation (PAMAM-G3) and examines the role of this surface functionalization in the modulation of the drug encapsulation and release properties of the prepared nanomaterials. Magnetic Fe_3O_4NT were obtained by reduction of α-Fe_2O_3 nanotubes, which were synthesized using a hydrothermal strategy. Pristine Fe_3O_4NT materials were subsequently grafted with PAMAM-G3 moieties using a silane coupling agent (GPTMS). The drug-loading and release properties of the pristine and PAMAM-modified nanomaterials were examined using silibinin (SIL) as model poorly soluble hydrophobic drug compound. Our results revealed that PAMAM incorporation exerted a favorable effect in the drug-encapsulating capacity and sustained release properties of Fe_3O_4NT, without altering the magnetic behavior of these systems compared to the pristine material. These

results are valuable for the design of novel nanomaterials with biomedical purposes and constitute a relevant outcome for our current and future research in this field.

Materials and methods

Materials

Poly(amido amine) dendrimer, ethylenediamine core, generation 3.0 (PAMAM-G3) solution 20 wt% in methanol, 3-(glycidyloxypropyl)trimethoxysilane (GPTMS, ≥98%), silibinin (SIL), $NH_4H_2PO_4$ were obtained from Sigma-Aldrich®. $FeCl_3 \cdot 6H_2O$, ethanol, nitric acid (HNO_3, 67%) and hydrochloric acid (HCl, 37%) and Na_2SO_4 were provided by Merck®. Toluene was dried over metallic sodium before use.

Synthesis of Fe_3O_4NT

To obtain the magnetic nanotubes, first the synthesis of hematite nanotubes (α-Fe_2O_3) was performed by means of a hydrothermal treatment of a mixture of salt solutions $FeCl_3 \cdot 6H_2O$, $NH_4H_2PO_4$ and Na_2SO_4 according to the work reported by Jia et al. [14, 15]. Briefly, aqueous solutions of $FeCl_3$, $NH_4H_2PO_4$ and $NaSO_4$ were mixed in 36:1.2:1 molar ratio at a total volume of 100 mL. The mixture was transferred into a hydrothermal reactor and heated at 220 °C for 48 h. After the hydrothermal treatment, the solid was washed with distilled water and ethanol. The solid was dried in a vacuum oven for 12 h at 80 °C to obtain α-Fe_2O_3 nanotubes. Subsequently, the α-Fe_2O_3 nanotubes were reduced under continuous flow of H_2 (5% v/v H_2/Ar) for 5 h at 360 °C (heating rate of 1 °C/min). This material was characterized by using different techniques, demonstrating the formation of Fe_3O_4 nanotubular structures (Fe_3O_4NT).

Synthesis of PAMAM-Fe_3O_4NT

Fe_3O_4NT were functionalized using 3-(glycidoxypropyl)methyldiethoxysilane (GPTMS) as coupling agent. For this purpose, 1.0 g of Fe_3O_4NT was dispersed in dry toluene for 30 min in an ultrasound bath; subsequently, 4.5 mmol of GPTMS was added, and the mixture was refluxed for 48 h. The modified nanotubes were filtered and washed exhaustively with toluene and acetone and then dried at 40 °C for 48 h in vacuum oven. This material was labeled as GPTMS-Fe_3O_4NT and was employed as starting material for PAMAM covalent attachment.

PAMAM covalent immobilization was carried out by placing 0.50 g of GPTMS-Fe_3O_4NT, 25 mL of dry DMSO and 0.5 mL of 0.81 mmol L^{-1} PAMAM-G3 in methanol solution into a round-bottom flask. The mixture was degassed with N_2 gas and stirred for 48 h at room temperature. The obtained solid was centrifuged with methanol and distilled water to remove the unreacted reagents and dried for 48 h at 40 °C in vacuum oven.

Materials characterization

XRD patterns were recorded on a Rigaku D/max-2500 diffractometer with the Fe Kα radiation at 35 kV and 150 mA. Infrared spectroscopy (FTIR) experiments were carried out on a Perkin Elmer 1760-X spectrometer using a range of 4000–400 cm^{-1} and KBr pellets. The N_2 adsorption–desorption isotherms at 77 K were performed on a Micromeritics ASAP 2010 apparatus. The specific surface areas were determined by the BET (Brunauer–Emmett–Teller) equation, using the adsorption data over the relative pressure range of 0.05–0.3, and the pore-size distributions were estimated using the BJH method. For surface area estimation and pore-size distribution, Fe_3O_4NT were degassed at 150 °C for 5 h, whereas PAMAM-Fe_3O_4NT were degassed at 25 °C (dye decomposition temperatures ~ 60 °C) for 5 h.

The TGA studies were conducted on a Mettler Toledo Thermogravimetric TGA/SDTA 851 using an N_2 flow of 25 mL min^{-1} and a heating rate of 5 °C min^{-1} from 25 to 800 °C. Dismissing the adsorbed water in Fe_3O_4, the mass loss percentage in TGA profiles allowed the determination of the PAMAM content in the prepared material by subtracting the mass loss in the PAMAM-Fe_3O_4NT system minus the mass loss in GPTMS-Fe_3O_4NT.

The morphology and size of the nanotubes were examined by Transmission Electron Microscopy (TEM) images. The micrographs were obtained using a Philips electron CM200 microscope with an energy dispersive analyzer and a digital camera coupled to a high-speed TVIPS FastScan F-114 model of 1024 × 1024 pixels and 12 bits. The samples for analysis were prepared by dispersion in ethanol/H_2O (1:1) and were deposited on a holey carbon Cu grid (300 mesh). TEM images were analyzed using

the imageJ software, considering >300 particles per sample.

Magnetic characterization of the nanomaterials was carried out in a vibrating sample magnetometer (VSM; MLVSM9 MagLab 9 T, Oxford Instrument). Magnetization curves were recorded at 290 K by first saturating the sample in a field of 5 T. Data are expressed in emu per gram of inorganic material (iron oxide). M_S was evaluated by extrapolating to infinite field the experimental results obtained in the high field range where the magnetization linearly increases with $1/H$.

Drug adsorption kinetic studies

Drug adsorption kinetic studies were carried out following the next general procedure: 10 mg of the solid materials (Fe_3O_4NT or PAMAM-Fe_3O_4NT) was dispersed in 2 mL of deionized water and put into a dialysis bag. After the dialysis bag was immersed into a flask containing 200 mL of drug solution (0.05 mg mL^{-1} of SIL). The drug solution was mechanically shaken at constant temperature (25 °C), in order to reach the equilibrium. Residual concentration of drug in the liquid solutions was measured with an UV–visible Spectrophotometer Spectroquant UV/Vis Spektralphotometer Pharo 300 Merck at the corresponding wavelength (287 nm) using previously recorded calibration curves data. Experiments were conducted in triplicate under identical conditions and were found reproducible (experimental error within 4%). The amount of adsorbed drug per gram of nanotube, q (mg g^{-1}) was calculated from the difference between the initial and final concentrations in solution after the respective contact times. Drug adsorption kinetic was fitted to different models using MATLAB R2011a (MathWorks, Inc., Massachusetts, USA) nonlinear regression tools.

In vitro drug release studies

SIL was incorporated into adsorbents by mixing 100 mg of ground samples of the nanotubes with 10 mL of aqueous solution of SIL (0.05 mg mL^{-1}) for 84 h at constant temperature (25 °C) in darkness under continuous mechanical shaking. After encapsulation, the powders were filtered by using 0.45 μm cellulose filter paper. Filtered powders were dried at 40 °C overnight to obtain drug-loaded Fe_3O_4NT and PAMAM-Fe_3O_4NT materials.

The in vitro drug release experiments were carried out by dispersing the prepared drug-loaded Fe_3O_4NT and PAMAM-Fe_3O_4NT materials into 75 mL of simulated body fluid (SBF, 0.14 mol L^{-1} Na$^+$, 5.0 mmol L^{-1} K$^+$, 2.5 mmol L^{-1} Ca^{2+}, 1.5 mmol L^{-1} Mg^{2+}, 0.15 mol L^{-1} Cl$^-$, 4.2 mmol L^{-1} HCO$_3^-$, 1 mmol L^{-1} HPO$_4^{2-}$ and 0.5 mmol L^{-1} SO$_4^{2-}$) at pH 7.3, leading to a final dispersion concentration of 3.33 g L^{-1}. 300 μL solution samples were consecutively taken in 2 h intervals and centrifuged in Amicon Ultra-0.5 Centrifugal Filter Unit with Ultracel-3 membrane (Merck). The drug content in the recovered filtered was analyzed by means of UV/VIS spectroscopy.

Cell viability assays

Cytotoxicity of the materials under study was evaluated using the Alamar Blue^{TM} cell viability assay on human embryonic kidney 293 cell line (HEK 293). Cells were incubated in 96-well plate with 30.000 cells per well on a solution of Dulbecco's Modified Eagle's Medium (DMEM 4.5 g L^{-1} glucose, 2 mmol L^{-1} glutamine, 0.11 g L^{-1} sodium pyruvate and 10% fetal bovine serum) and dispersions of Fe_3O_4NT and PAMAM-Fe_3O_4NT (10–500 μg mL^{-1}) for 24 h at 37 °C and 5% CO_2. Then, the medium was removed and replaced by medium with Alamar blue reagent. Cells were incubated 3 h, and finally the fluorescence was measured in a NOVOstar (BGM, Germany) multiplate reader at 580 nm. Comparison with control groups was performed using standard one-way ANOVA and $p < 0.05$ for significant differences from cell survival control.

Results and discussion

This work describes the surface modification of magnetic Fe_3O_4NT with PAMAM dendrimers of the third generation, as potential modulators of the drug-encapsulating and release properties of these nanomaterials. Pristine Fe_3O_4NT were obtained by reduction of α-Fe_2O_3 nanotubes that were previously synthesized using a hydrothermal procedure. Pristine Fe_3O_4NT were then subjected to a surface functionalization with the GPTMS silane agent and further coupled with PAMAM-G3 dendrimers through a ring opening reaction promoted by the primary amine groups of PAMAM-G3 acting as nucleophiles (Fig. 1). The presence of magnetite in

Fe$_3$O$_4$NT and PAMAM-Fe$_3$O$_4$NT systems was verified from XRD experiments, which revealed the appearance of standard patterns for magnetite in both materials [(111), (220), (311), (222), (400), (511) and (440), JCPDS No. 19-0629]. These characteristic signals differ from the XRD pattern corresponding to the α-Fe$_2$O$_3$ precursor, which presented major characteristic peaks associated to hematite [(012), (104), (110), (113), (024), (116), (018) and (214), JCPDS No. 33-0664], thus confirming the success of the reduction procedure (Fig. 2). No significant differences were observed in the XRD patterns of pristine and PAMAM-modified Fe$_3$O$_4$NT materials, which evidenced that PAMAM grafting did not induce changes in the crystalline structure of magnetite.
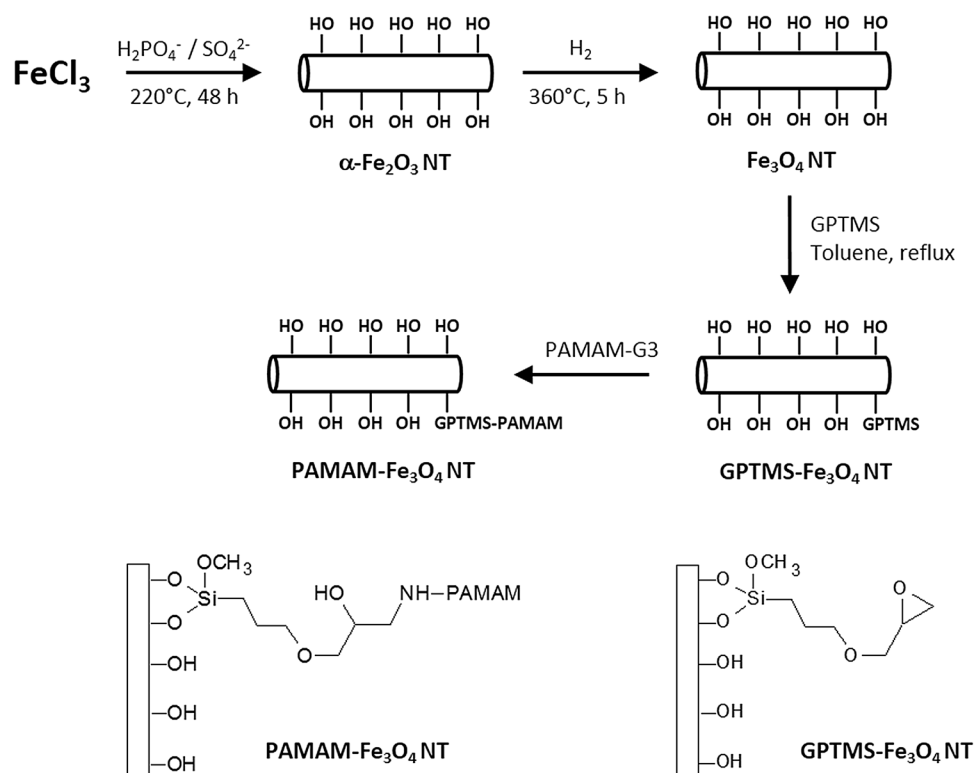
FTIR spectra of Fe$_3$O$_4$NT, GPTMS-Fe$_3$O$_4$NT and PAMAM-Fe$_3$O$_4$NT materials are reported in Fig. 2 and were employed to verify the covalent attachment of organic moieties to Fe$_3$O$_4$NT. Pristine Fe$_3$O$_4$NT showed characteristic IR bands at 3340–3000 cm^{-1}, corresponding to the stretching mode associated to surface hydroxyl groups and adsorbed water molecules, 1628 cm^{-1} attributed to the OH bending mode and 574 cm^{-1} associated to the Fe–O stretching in the magnetite lattice [34, 35]. GPTMS-Fe$_3$O$_4$NT showed peaks corresponding to aliphatic C–H stretching in the region comprised between 2800 and 2900 cm^{-1} and a weak signal around 1100 cm^{-1} associated to Si–O stretching. PAMAM-Fe$_3$O$_4$NT showed characteristic bands of aliphatic C–H stretching modes centered at 2912 and 2849 cm^{-1}, amide C=O stretching mode centered at 1638 cm^{-1}, NH bending mode at 1541 cm^{-1} and a C–N vibration at 1106 cm^{-1} [36]. TGA analysis was further employed to estimate the percentage of PAMAM grafting in the prepared material by subtracting the mass loss percentage observed in the PAMAM-Fe$_3$O$_4$NT system minus the mass loss percentage measured in the GPTSM-Fe$_3$O$_4$NT precursor. Our results revealed a PAMAM grafting percentage of 16.8 wt%, corresponding to a dendrimer content of 24.3 μmol g^{-1}. Further experiments were carried out aimed at characterizing the morphology and magnetic properties of the prepared materials, as described in the following section.

Morphology and magnetic properties of Fe$_3$O$_4$NT and PAMAM-Fe$_3$O$_4$NT

TEM analyses were employed to examine the morphology of pristine and PAMAM-modified Fe$_3$O$_4$NT materials (Fig. 3). According to TEM images, the prepared materials exhibit nanotubular shapes with
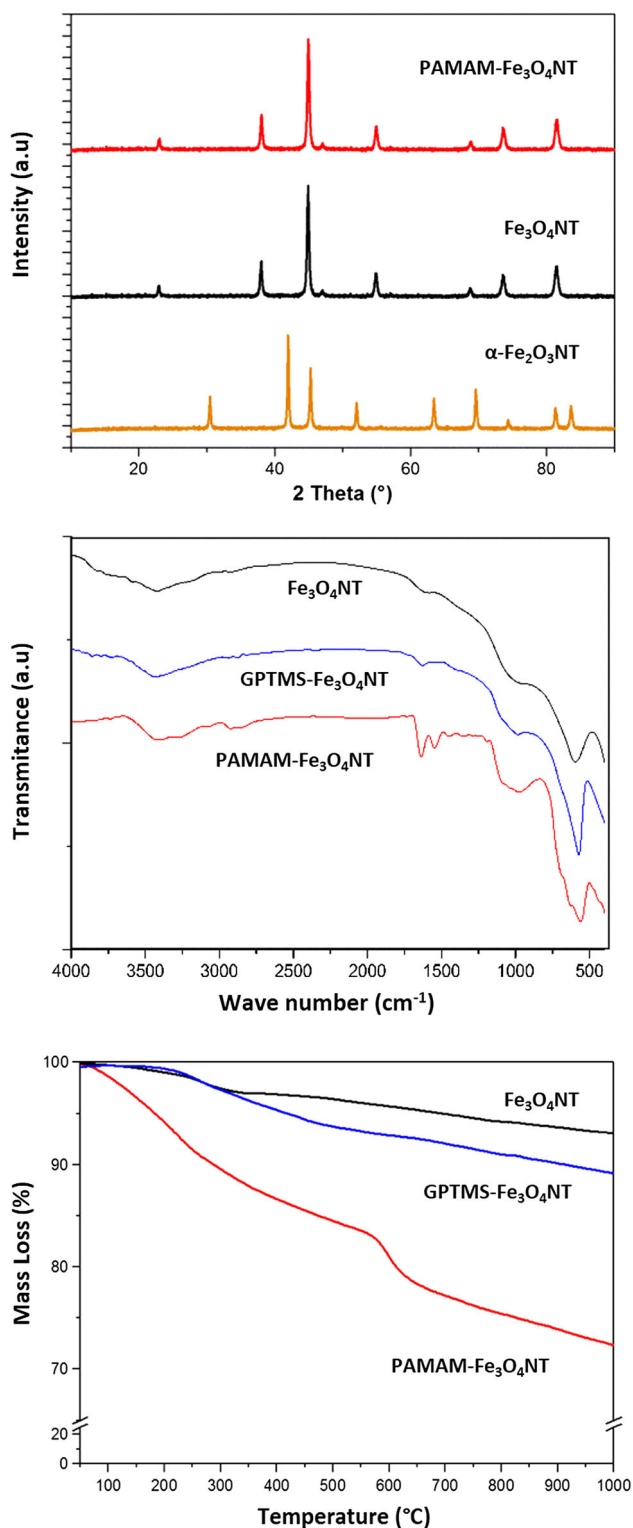

Figure 1 Synthesis of PAMAM-modified Fe$_3$O$_4$NT.

Figure 2 XRD patterns, FTIR spectra and TGA profiles for Fe_3O_4NT related materials.

dimensions of the prepared nanotubes are significantly larger than the average diameter of PAMAM-G3 (3.6 nm), thus enabling the functionalization of Fe_3O_4NT on both internal and external nanotube surfaces. However, the direct observation of the organic moieties attached to Fe_3O_4NT was not possible to achieve considering that TEM resolution is in the range of PAMAM size. An indirect evidence of the partial coverage of internal nanotube cavities with PAMAM moieties was obtained from nitrogen adsorption–desorption isotherms as displayed in Fig. 4. In the case of native Fe_3O_4NT, the adsorption isotherm showed a type IV mesoporous profile with a characteristic hysteresis loop at $P/P^0 = 0.45–1.0$ of H1-type, which is customarily associated to mesoporous materials with uniform pores. In the case of PAMAM-Fe_3O_4NT, the isotherm showed a similar shape but revealed a decrease in the mesopore size and surface area as compared to the pristine material, thus suggesting a partial coverage of the nanotube pore surface with PAMAM molecules, leading to a wall thickness increase. Estimated pore diameters for the Fe_3O_4NT and PAMAM-Fe_3O_4NT ranged between 19 and 33 nm, which correspond to suitable pore sizes to allow the entrance and encapsulation of medium to large organic compounds, such as SIL.

To assess the magnetic properties of Fe_3O_4NT and PAMAM-Fe_3O_4NT materials, VSM magnetic hysteresis measurements were carried out at 290 K (Fig. 5). The saturation magnetizations (M_s) of Fe_3O_4NT and PAMAM-Fe_3O_4NT were found to be 67 and 59 emu g^{-1}, respectively. Hysteresis loop measurements demonstrated that magnetic nanotubes exhibited a weak ferromagnetic behavior. Fe_3O_4NT and PAMAM-Fe_3O_4NT presented remanent magnetization (M_r) and coercivity (H_c), with M_r values of 17 and 14 emu g^{-1} and H_c values of 260 and 240 Oe for Fe_3O_4NT and PAMAM-Fe_3O_4NT materials, respectively. This values of remanent magnetization and coercivity are typical of magnetite and maghemite [37, 38]. Several authors have shown that coercivity is related to the shape anisotropy of tubular structure and the magneto-crystalline anisotropy of the particles [39] and for Fe_3O_4 nanotubular materials H_c values in the range of 193–205 Oe have been reported [37, 40].

In summary, TEM analysis, nitrogen adsorption–desorption experiments and VSM magnetic measurements confirmed the nanometric size, nanotubular shape and magnetic behavior of Fe_3O_4NT and PAMAM-Fe_3O_4NT materials, which is a valuable

average lengths of 280 and 286 nm, and average diameters of 151 and 159 nm, for Fe_3O_4NT and PAMAM-Fe_3O_4NT systems, respectively. The

Figure 3 TEM images and size distribution data for **a** Fe$_3$O$_4$NT and **b** PAMAM-Fe$_3$O$_4$NT.
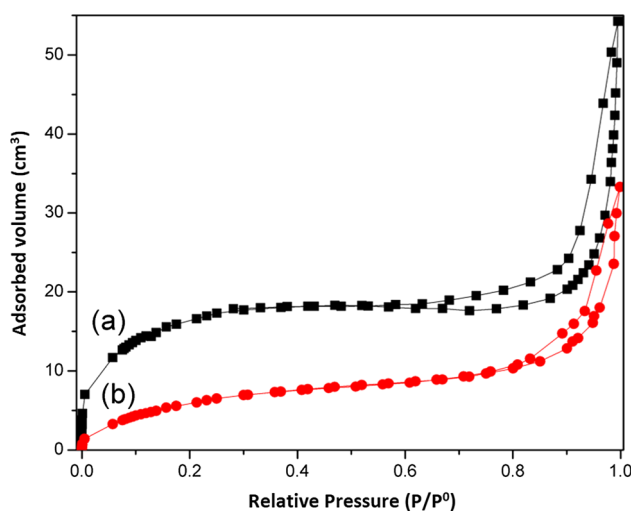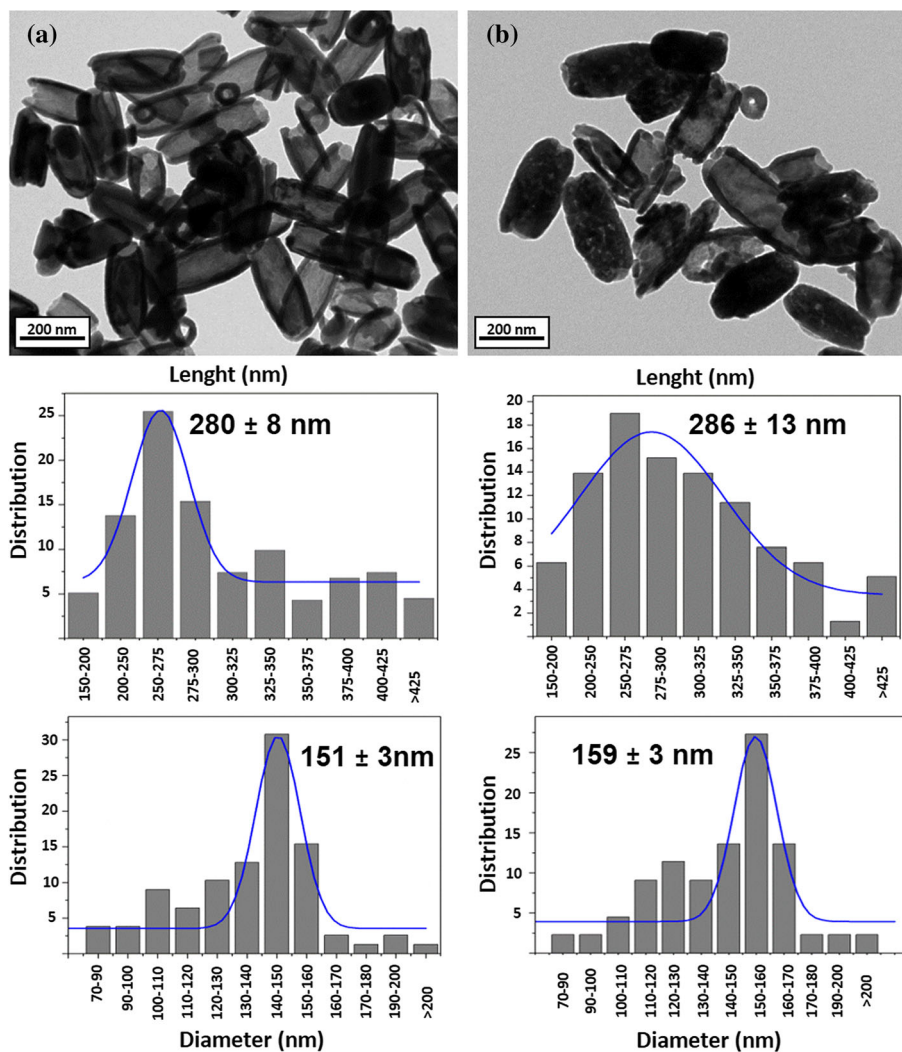

Figure 4 Nitrogen adsorption–desorption isotherms for *a* Fe$_3$O$_4$-NT and *b* PAMAM-Fe$_3$O$_4$NT.

result to further examine the properties of these systems as potentials carriers for drug encapsulation and sustained release, as described next.

Drug adsorption kinetic studies

Drug adsorption kinetic studies were carried out to examine the effect of PAMAM incorporation on the drug encapsulation and release properties of Fe$_3$O$_4$-NT using SIL as model drug compound. SIL is a natural polyphenolic flavonoid with hepatoprotective and antitumoral properties [41, 42]. This compound is isolated from the plant milk thistle Silybum marianum and has shown a strong efficacy in various human cancer cell lines and also in several animal models of cancer [43, 44]. However, the effectiveness of this drug is seriously limited by its low solubility in water, and low bioavailability after oral

Figure 5 Magnetic hysteresis measurements for **a** Fe_3O_4NT and **b** PAMAM-Fe_3O_4NT.
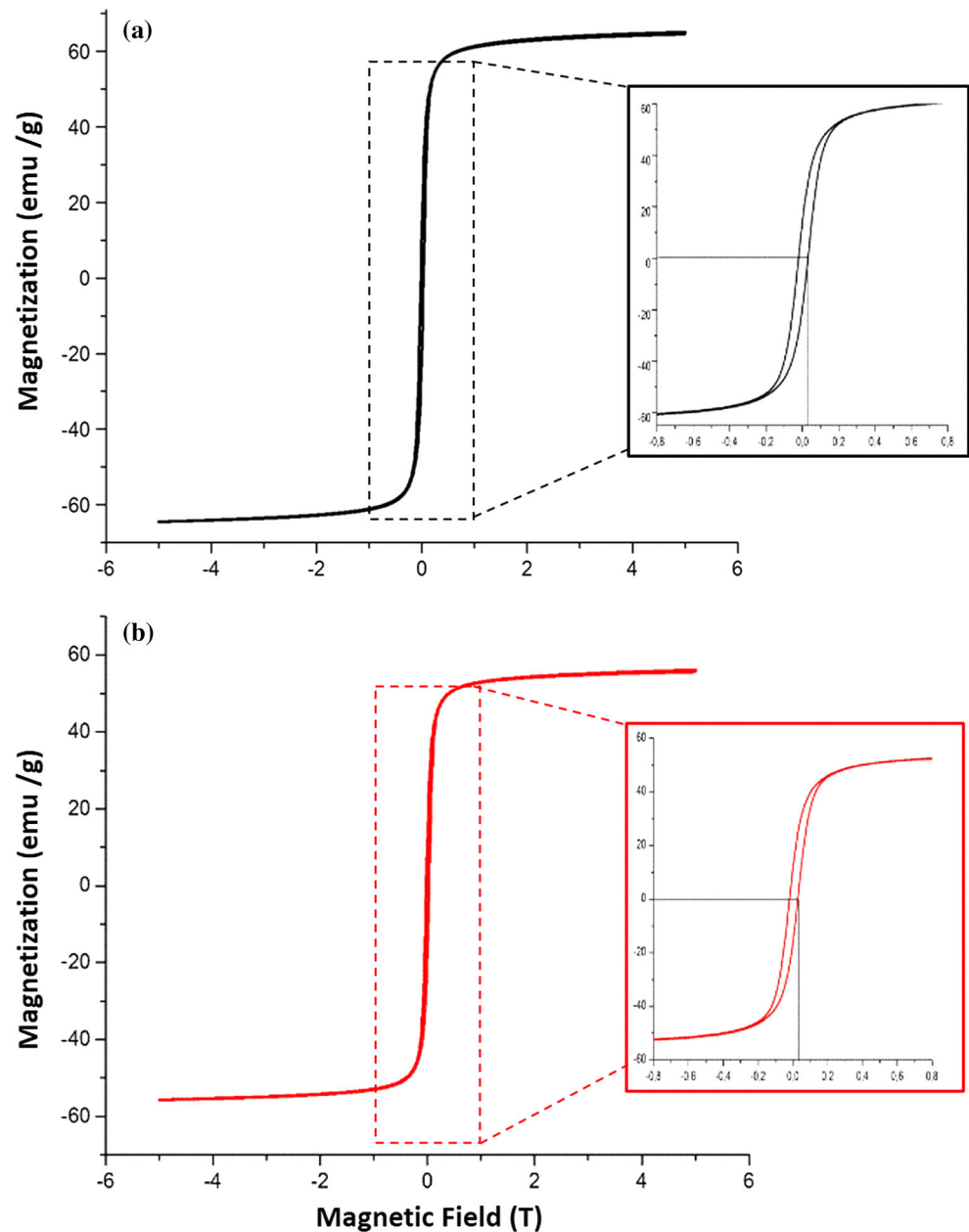
administration. To overcome these drawbacks different experimental strategies have been assayed in the past, such as the preparation of β-cyclodextrin inclusion complexes, phospholipid complexes, nanosuspensions, porous silica nanoparticles, liposomes and microencapsulation in polymeric matrices [45–50]. Nevertheless, despite the relative success in this subject, some of these formulations are degraded rapidly, do not produce sustained drug release or have limited physical or chemical stability during storage, which encourages the search for novel

nanocarriers for SIL and its derivatives, as described in this work.

Kinetic profiles for SIL adsorption into Fe_3O_4NT and PAMAM-Fe_3O_4NT materials were obtained by registering the amount of drug adsorbed (mg g^{-1}) at different times during the course of 80–100 h, as shown in Fig. 6. Experimental profiles revealed that SIL encapsulation occurs at low rates and reached equilibrium after 60 h of contact in both systems. Kinetic parameters for the SIL adsorption were obtained from fitting the experimental data to the
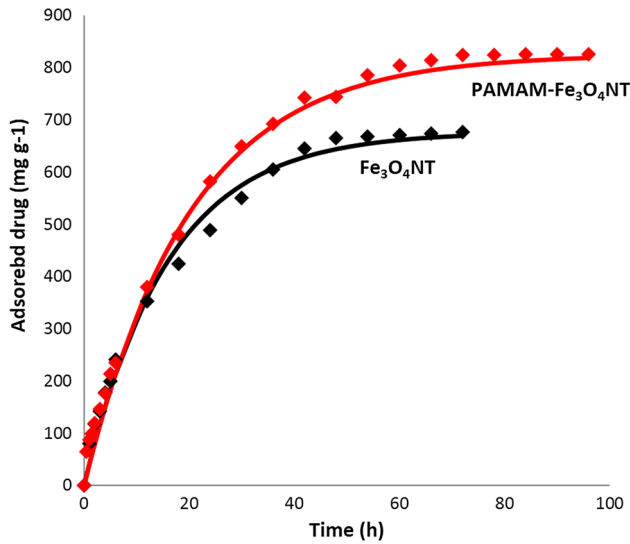
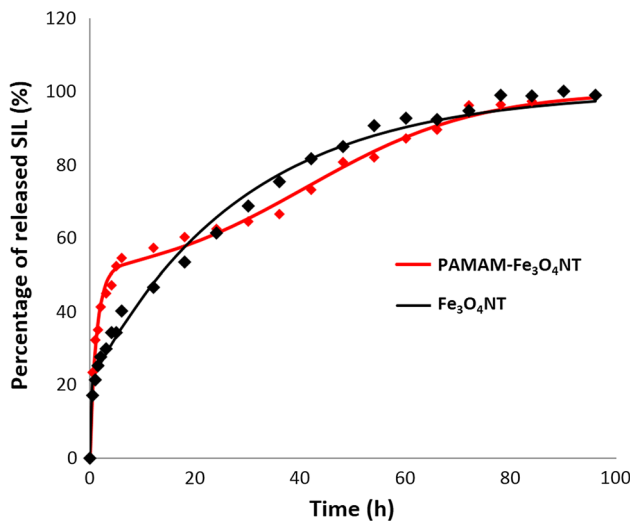**Figure 6** Drug adsorption kinetic profiles for SIL encapsulation in Fe_3O_4NT and $PAMAM-Fe_3O_4NT$.

Figure 7 Drug release kinetic profiles for the exit of SIL from Fe_3O_4NT and $PAMAM-Fe_3O_4NT$.

pseudo-first-order Lagergren's model, as described in following equation [10, 51]

Lagergren model $\quad q_t = q_e \left(1 - e^{-k_1 t}\right) \qquad (1)$

where q_t and q_e are the amount of adsorbed drug $(mg\ g^{-1})$ at the time t and at the equilibrium, respectively, and k_1 is the pseudo-first-order rate constant (h^{-1}). Fitting results revealed that both systems present similar pseudo-first-order rate constants with values of 0.052 and 0.062 h^{-1} for Fe_3O_4NT and $PAMAM-Fe_3O_4NT$ materials, respectively. Additionally, kinetic adsorption profiles revealed a favorable effect in the drug-encapsulating capacity of Fe_3O_4NT

after PAMAM incorporation, with a maximum amount of adsorbed SIL of 825 mg g^{-1} in the PAMAM-modified system compared to 675 mg g^{-1} in the pristine material, representing a 22% drug-loading increase. The measured SIL adsorption capability of $PAMAM-Fe_3O_4NT$ exceeded significantly the performance of PAMAM-grafted alumina and titania nanotubes that were recently synthetized by us, which showed drug-loading capacities in the range of 5–40 mg g^{-1} [26, 27], which is a promising outcome for the use of Fe_3O_4NT and $PAMAM-Fe_3O_4NT$ materials as platforms for the future design of more efficient drug carriers for insoluble drugs such as SIL.

Regarding the nature of the adsorption phenomena, SIL interaction with pristine and PAMAM-modified Fe_3O_4NT can take place through a combination of van der Waals, dipole–dipole and hydrogen-bonding interactions, involving the apolar, polar and hydrogen donor/acceptor groups of SIL, respectively. These interactions can occur on both the internal and external surface of the nanotubular materials. Nevertheless, considering the slow rate of SIL adsorption, internal drug complexation is expected to predominate over external association.

Drug release kinetic studies

In vitro drug release kinetic studies were performed to obtain information about the characteristics of SIL release from Fe_3O_4NT and $PAMAM-Fe_3O_4NT$ materials. The accumulative percentage of drug released from each nanomaterial during the course of 100 h is reported in Fig. 7. Release kinetic data were adjusted to two different mathematical models, namely first-order and Gallagher–Corrigan models to account for one-step and two-step release profiles, respectively [52–54]. Best-fit parameters for each system are provided in Table 1.

First order $\quad \dfrac{M_t}{M_\infty} = 100 - e^{b-kt} \qquad (2)$

where M_t/M_∞ is the cumulative drug release percentage at time t and at infinite, k is the first-order kinetic constant and b is a constant.

Gallagher − Corrigan

$$f_t = f_B \left(1 - e^{-k_1 t}\right) + \left(f_{max} - f_B\right)\left(\frac{e^{k_2 t - k_2 t_{2max}}}{1 + e^{k_2 t - k_2 t_{2max}}}\right) \qquad (3)$$

Table 1 Kinetic models equations and best-fit parameters for the release of SIL from pristine and PAMAM-modified Fe₃O₄NT

System	Model and parameters			
SIL: Fe₃O₄NT	$\frac{M_t}{M_\infty} = 100 - e^{b-kt}$			
	k (h^{-1})		b	
	3.5×10^{-2}		4.38	
SIL: PAMAM-Fe₃O₄NT	$f_t = f_B\left(1 - e^{-k_1 t}\right) + (f_{max} - f_B)\left(\frac{e^{k_2 t - k_2 t_{2max}}}{1 + e^{k_2 t - k_2 t_{2max}}}\right)$			
	k_1 (h^{-1})	k_2 (h^{-1})	f_B	t_{2max} (h)
	0.78	6.1×10^{-2}	47.3	41

where f_t is the cumulative percentage of released drug at a time t, f_B is the fraction of drug released during the first stage, k_1 is the first-order kinetic constant of the first stage of release, k_2 is the kinetic constant for the second stage of release, and t_{2max} the time to maximum drug release rate.

In both pristine and PAMAM-modified Fe₃O₄NT, the release rate is higher at the initial portion of the experiments, thus evidencing a strong influence of the concentration of SIL in the bulk solution. This result suggests that drug release is diffusion controlled in both systems. In the case of Fe₃O₄NT, experimental data followed a typical first-order kinetics, corresponding to a one-step release of the drug from this nanomaterial, with a kinetic constant of $k = 3.5 \times 10^{-2}$ h^{-1}. In the case of PAMAM-Fe₃O₄NT, release data were better fitted to a Gallagher–Corrigan model, thus accounting for a two-stage release process, with kinetic constants $k_1 = 0.78$ and $k_2 = 6.1 \times 10^{-2}$ h^{-1}. These results can be roughly interpreted as the additive contribution of a fast initial release of SIL molecules from PAMAM moieties, followed by a slow exit of the drug from the Fe₃O₄NT matrix. At 5 h of release time, a 34% of encapsulated SIL was liberated from Fe₃O₄NT material, whereas a 52% of the drug was released from PAMAM-Fe₃O₄NT. At 20 h of release, the exit profiles of Fe₃O₄NT and PAMAM-Fe₃O₄NT materials intersect and equal the amount of released drug at 53–57%. After this time, the exit of the drug from PAMAM-Fe₃O₄NT becomes slower than Fe₃O₄NT, thus suggesting that PAMAM incorporation induced a more sustained release of the remaining adsorbed drug in the nanotube framework (47–43%), which represents the exit of 317 and 387 mg of SIL for Fe₃O₄NT and PAMAM-Fe₃O₄NT materials, respectively. Thus, even though the liberation of SIL occurs faster in the first stage of release from PAMAM-Fe₃O₄NT, the performance of this material for the sustained release of the second half of the encapsulated drug is superior in the

PAMAM-modified material compared to pristine Fe₃O₄NT.

Cell viability studies

In order to evaluate the cytotoxicity of magnetic nanotube materials, standard Alamar Blue cell viability assays were performed by using human embryonic kidney 293 cell line. Figure 8 displays the results of the cell viability assays, showing the percentage of cell survival versus the concentration of magnetic Fe₃O₄NT and PAMAM-Fe₃O₄NT materials. The results were compared with a positive control (C+; 100% of cell viability), and Triton-treated cell cultures as a negative control (C−), which were used as reference systems for comparative purposes. The results showed that both Fe₃O₄NT and PAMAM-Fe₃O₄NT nanomaterials, caused a small decrease in the cell proliferation in an independent concentration manner, with cytotoxicity behaviors similar to other magnetic nanoparticles [55–57], showing that these
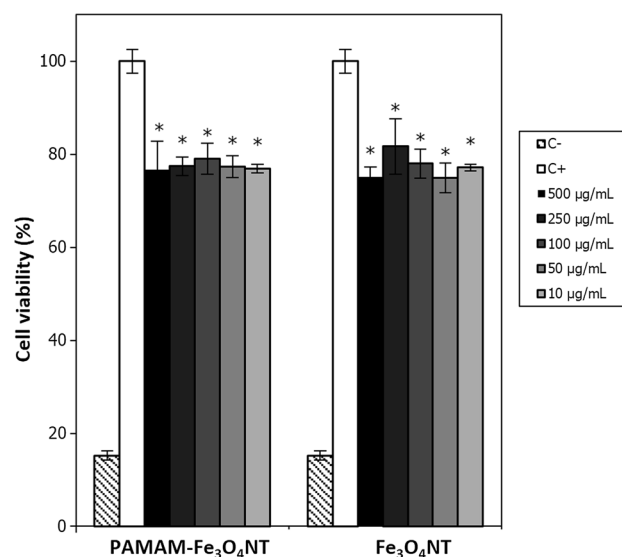

Figure 8 Standard Alamar Blue cell viability assays for Fe₃O₄NT and PAMAM-Fe₃O₄NT using embryonic kidney 293 cell lines.

magnetic nanotubes are promising biocompatible materials for drug delivery.

Conclusions

The synthesis of Fe_3O_4NT and $PAMAM-Fe_3O_4NT$ nanomaterials was carried out, leading to novel PAMAM-modified materials with a substitution percentage of 16.8%, which retained the nanotubular morphology, magnetic properties and low cytotoxicity of pristine Fe_3O_4NT materials. Drug adsorption kinetic studies using the poorly soluble drug silibinin revealed that PAMAM grafting induced a favorable effect on the drug-loading capacity of Fe_3O_4NT by increasing the amount of adsorbed drug from 675 mg g^{-1} in the pristine material to 825 mg g^{-1} in the PAMAM-modified system. The drug adsorption performance of Fe_3O_4NT and $PAMAM-Fe_3O_4NT$ materials largely exceeds the drug-loading capacity of similar systems and constitutes a promising result for future drug-delivery applications. Regarding to drug release properties, PAMAM grafting induced a more sustained release of the second half of the adsorbed drug, while the first half is released faster from the modified material compared to pristine Fe_3O_4NT. The auspicious results discussed in the present report constitute the initial efforts of our group in designing novel PAMAM-modified magnetic nanomaterials with enhanced drug-loading capacities for a diversity of insoluble therapeutics, which will be addressed in our future contributions.

Acknowledgements

Compliance with ethical standards

Conflict of interest   The authors declare no conflict of interest.

Electronic supplementary material: The online version of this article (doi:10.1007/s10853-017-1140-4) contains supplementary material, which is available to authorized users.

References

[1] Zhang L, Gu FX, Chan JM, Wang AZ, Langer RS, Farokhzad OC (2008) Nanoparticles in medicine: therapeutic applications and developments. Clin Pharmacol Ther 83(5):761–769. doi:10.1038/sj.clpt.6100400

[2] Faraji AH, Wipf P (2009) Nanoparticles in cellular drug delivery. Bioorg Med Chem 17(8):2950–2962. doi:10.1016/j.bmc.2009.02.043

[3] Kievit FM, Zhang MQ (2011) Surface engineering of iron oxide nanoparticles for targeted cancer therapy. Acc Chem Res 44(10):853–862. doi:10.1021/ar2000277

[4] Yu MK, Park J, Jon S (2012) Targeting strategies for multifunctional nanoparticles in cancer imaging and therapy. Theranostics 2(1):3–44. doi:10.7150/thno.3463

[5] Liu Z, Sun XM, Nakayama-Ratchford N, Dai HJ (2007) Supramolecular chemistry on water-soluble carbon nanotubes for drug loading and delivery. ACS Nano 1(1):50–56. doi:10.1021/nn700040t

[6] Goldberg M, Langer R, Jia XQ (2007) Nanostructured materials for applications in drug delivery and tissue engineering. J Biomater Sci Polym E 18(3):241–268. doi:10.1163/156856207779996931

[7] Song YY, Schmidt-Stein F, Bauer S, Schmuki P (2009) Amphiphilic TiO_2 nanotube arrays: an actively controllable drug delivery system. J Am Chem Soc 131(12):4230–4232. doi:10.1021/ja810130h

[8] Popat KC, Eltgroth M, La Tempa TJ, Grimes CA, Desai TA (2007) Titania nanotubes: A novel platform for drug-eluting coatings for medical implants? Small 3(11):1878–1881. doi:10.1002/smll.200700412

[9] Li XM, Wang L, Fan YB, Feng QL, Cui FZ (2012) Biocompatibility and toxicity of nanoparticles and nanotubes. J Nanomater 2012:548389. doi:10.1155/2012/548389

[10] Wang QJ, Liu RJ, Shen XQ, Zou LL, Wu DM (2014) Mesoporous iron oxide nanofibers and their loading capacity of curcumin. J Nanosci Nanotechnol 14(4):2871–2877. doi:10.1166/jnn.2014.8624

[11] Fratila RM, Rivera-Fernandez S, de la Fuente JM (2015) Shape matters: synthesis and biomedical applications of high aspect ratio magnetic nanomaterials. Nanoscale 7(18):8233–8260. doi:10.1039/c5nr01100k

[12] Horst MF, Lassalle V, Ferreira ML (2015) Nanosized magnetite in low cost materials for remediation of water polluted with toxic metals, azo- and antraquinonic dyes. Front Environ Sci Eng 9(5):746–769. doi:10.1007/s11783-015-0814-x

[13] Keerthana DS, Namratha K, Byrappa K, Yathirajan HS (2015) Facile one-step fabrication of magnetite particles under mild hydrothermal conditions. J Magn Magn Mater 378:551–557. doi:10.1016/j.jmmm.2014.10.176

[14] Jia CJ, Sun LD, Yan ZG, You LP, Luo F, Han XD, Pang YC, Zhang Z, Yan CH (2005) Iron oxide nanotubes: single-crystalline iron oxide nanotubes. Angew Chem Int Ed 44(28):4328–4333. doi:10.1002/anie.200463038

[15] Jia CJ, Sun LD, Luo F, Han XD, Heyderman LJ, Yan ZG, Yan CH, Zheng K, Zhang Z, Takano M, Hayashi N, Eltschka M, Klaui M, Rudiger U, Kasama T, Cervera-Gontard L, Dunin-Borkowski RE, Tzvetkov G, Raabe J (2008) Large-scale synthesis of single-crystalline iron oxide magnetic nanorings. J Am Chem Soc 130(50):16968–16977. doi:10.1021/ja805152t

[16] Mizutani N, Iwasaki T, Watano S, Yanagida T, Kawai T (2010) Size control of magnetite nanoparticles in hydrothermal synthesis by coexistence of lactate and sulfate ions. Curr Appl Phys 10(3):801–806. doi:10.1016/j.cap.2009.09.018

[17] Yue ZG, Wei W, You ZX, Yang QZ, Yue H, Su ZG, Ma GH (2011) Iron oxide nanotubes for magnetically guided delivery and pH-activated release of insoluble anticancer drugs. Adv Funct Mater 21(18):3446–3453. doi:10.1002/adfm.201100510

[18] Park J, Kadasala NR, Abouelmagd SA, Castanares MA, Collins DS, Wei A, Yeo Y (2016) Polymer-iron oxide composite nanoparticles for EPR-independent drug delivery. Biomaterials 101:285–295. doi:10.1016/j.biomaterials.2016.06.007

[19] Gonzalez-Moragas L, Yu SM, Carenza E, Laromaine A, Roig A (2015) Protective effects of bovine serum albumin on superparamagnetic iron oxide nanoparticles evaluated in the nematode Caenorhabditis elegans. ACS Biomater Sci Eng 1(11):1129–1138. doi:10.1021/acsbiomaterials.5b00253

[20] Castillo PM, de la Mata M, Casula MF, Sanchez-Alcazar JA, Zaderenko AP (2014) PEGylated versus non-PEGylated magnetic nanoparticles as camptothecin delivery system. Beilstein J Nanotechnol 5:1312–1319. doi:10.3762/bjnano.5.144

[21] Mahdavi M, Bin Ahmad M, Haron MJ, Namvar F, Nadi B, Ab Rahman MZ, Amin J (2013) Synthesis, surface modification and characterisation of biocompatible magnetic iron oxide nanoparticles for biomedical applications. Molecules 18(7):7533–7548. doi:10.3390/molecules18077533

[22] Tajabadi M, Khosroshahi ME, Bonakdar S (2013) An efficient method of SPION synthesis coated with third generation PAMAM dendrimer. Colloid Surf A 431:18–26. doi:10.1016/j.colsurfa.2013.04.003

[23] Shi X, Wang SH, Swanson SD, Ge S, Cao Z, Van Antwerp ME, Landmark KJ, Baker JR (2008) Dendrimer-functionalized shell-crosslinked iron oxide nanoparticles for in-vivo magnetic resonance imaging of tumors. Adv Mater 20(9):1671–1678. doi:10.1002/adma.200702770

[24] Strable E, Bulte JWM, Moskowitz B, Vivekanandan K, Allen M, Douglas T (2001) Synthesis and characterization of soluble iron oxide–dendrimer composites. Chem Mater 13(6):2201–2209. doi:10.1021/cm010125i

[25] Deriu MA, Popescu LM, Ottaviani MF, Danani A, Piticescu RM (2016) Iron oxide/PAMAM nanostructured hybrids: combined computational and experimental studies. J Mater Sci 51(4):1996–2007. doi:10.1007/s10853-015-9509-8

[26] Campos CH, Diaz CF, Guzman JL, Alderete JB, Torres CC, Jimenez VA (2016) PAMAM-conjugated alumina nanotubes as novel noncytotoxic nanocarriers with enhanced drug loading and releasing performances. Macromol Chem Phys 217(15):1712–1722. doi:10.1002/macp.201600136

[27] Torres CC, Campos CH, Diaz C, Jimenez VA, Vidal F, Guzman L, Alderete JB (2016) PAMAM-grafted TiO$_2$ nanotubes as novel versatile materials for drug delivery applications. Mater Sci Eng C J 65:164–171. doi:10.1016/j.msec.2016.03.104

[28] Devarakonda B, Hill RA, de Villiers MM (2004) The effect of PAMAM dendrimer generation size and surface functional group on the aqueous solubility of nifedipine. Int J Pharm 284(1–2):133–140. doi:10.1016/j.ijpharm.2004.07.006

[29] Barra PA, Barraza L, Jimenez VA, Gavin JA, Alderete JB (2014) Complexation of mefenamic acid by low-generation PAMAM dendrimers: insight from NMR spectroscopy studies and molecular dynamics simulations. Macromol Chem Phys 215(4):372–383. doi:10.1002/macp.201300398

[30] Fant K, Esbjorner EK, Jenkins A, Grossel MC, Lincoln P, Norden B (2010) Effects of PEGylation and acetylation of PAMAM dendrimers on DNA binding, cytotoxicity and in vitro transfection efficiency. Mol Pharm 7(5):1734–1746. doi:10.1021/mp1001312

[31] Kolhatkar RB, Kitchens KM, Swaan PW, Ghandehari H (2007) Surface acetylation of polyamidoamine (PAMAM) dendrimers decreases cytotoxicity while maintaining membrane permeability. Bioconjugate Chem 18(6):2054–2060. doi:10.1021/bc0603889

[32] Markatou E, Gionis V, Chryssikos GD, Hatziantoniou S, Georgopoulos A, Demetzos C (2007) Molecular interactions between dimethoxycurcumin and Pamam dendrimer carriers. Int J Pharm 339(1–2):231–236. doi:10.1016/j.ijpharm.2007.02.037

[33] Borowska K, Wolowiec S, Rubaj A, Glowniak K, Sieniawska E, Radej S (2012) Effect of polyamidoamine dendrimer G3 and G4 on skin permeation of 8-methoxypsoralene-in vivo study. Int J Pharm 426(1–2):280–283. doi:10.1016/j.ijpharm.2012.01.041

[34] Savic AB, Cokesa D, Lazarevic S, Jokic B, Janackovic D, Petrovic R, Zivkovic LS (2016) Tailoring of magnetite powder properties for enhanced phosphate removal: effect of

PEG addition in the synthesis process. Powder Technol 301:511–519. doi:10.1016/j.powtec.2016.06.028

[35] Rajput S, Pittman CU, Mohan D (2016) Magnetic magnetite (Fe_3O_4) nanoparticle synthesis and applications for lead (Pb^{2+}) and chromium (Cr^{6+}) removal from water. J Colloid Interface Sci 468:334–346. doi:10.1016/j.jcis.2015.12.008

[36] Mansourpanah Y, Jafari Z (2015) Efficacy of different generations and concentrations of PAMAM-NH2 on the performance and structure of TFC membranes. React Funct Polym 93:178–189. doi:10.1016/j.reactfunctpolym.2015.04.010

[37] Wu W, Xiao XH, Zhang SF, Zhou JA, Fan LX, Ren F, Jiang CZ (2010) Large-scale and controlled synthesis of iron oxide magnetic short nanotubes: shape evolution, growth mechanism, and magnetic properties. J Phys Chem C 114(39):16092–16103. doi:10.1021/jp1010154

[38] Gandha K, Mohapatra J, Hossain MK, Elkins K, Poudyal N, Rajeshwar K, Liu JP (2016) Mesoporous iron oxide nanowires: synthesis, magnetic and photocatalytic properties. RSC Adv 6(93):90537–90546. doi:10.1039/c6ra18530d

[39] Han XF, Shamaila S, Sharif R, Chen JY, Liu HR, Liu DP (2009) Structural and magnetic properties of various ferromagnetic nanotubes. Adv Mater 21(45):4619–4624. doi:10.1002/adma.200901065

[40] Wu W, Xiao XH, Ren F, Zhang SF, Jiang CZ (2012) A comparative study of the magnetic behavior of single and tubular clustered magnetite nanoparticles. J Low Temp Phys 168(5):306–313. doi:10.1007/s10909-012-0634-3

[41] Dehmlow C, Erhard J, deGroot H (1996) Inhibition of Kupffer cell functions as an explanation for the hepatoprotective properties of silibinin. Hepatology 23(4):749–754. doi:10.1002/hep.510230415

[42] Deep G, Agarwal R (2010) Antimetastatic efficacy of silibinin: molecular mechanisms and therapeutic potential against cancer. Cancer Metastab Rev 29(3):447–463. doi:10.1007/s10555-010-9237-0

[43] Singh RP, Deep G, Chittezhath M, Kaur M, Dwyer-Nield LD, Malkinson AM, Agarwal R (2006) Effect of silibinin on the growth and progression of primary lung tumors in mice. J Natl Cancer I 98(12):846–855. doi:10.1093/jnci/djj231

[44] Singh RP, Agarwal R (2006) Prostate cancer chemoprevention by silibinin: bench to bedside. Mol Carcinog 45(6):436–442. doi:10.1002/mc.20223

[45] Cao X, Deng W, Fu M, Zhu Y, Liu H, Wang L, Zeng J, Wei Y, Xu X, Yu J (2013) Seventy-two-hour release formulation of the poorly soluble drug silybin based on porous silica nanoparticles: in vitro release kinetics and in vitro/in vivo correlations in beagle dogs. Eur J Pharm Sci 48(1–2):64–71. doi:10.1016/j.ejps.2012.10.012

[46] Kumar N, Rai A, Reddy ND, Raj PV, Jain P, Deshpande P, Mathew G, Kutty NG, Udupa N, Rao CM (2014) Silymarin liposomes improves oral bioavailability of silybin besides targeting hepatocytes, and immune cells. Pharm Rep 66(5):788–798. doi:10.1016/j.pharep.2014.04.007

[47] Nguyen M-H, Yu H, Dong B, Hadinoto K (2016) A supersaturating delivery system of silibinin exhibiting high payload achieved by amorphous nano-complexation with chitosan. Eur J Pharm Sci 89:163–171. doi:10.1016/j.ejps.2016.04.036

[48] Ripoli M, Angelico R, Sacco P, Ceglie A, Mangia A (2016) Phytoliposome-based silibinin delivery system as a promising strategy to prevent hepatitis C virus infection. J Biomed Nanotechnol 12(4):770–780. doi:10.1166/jbn.2016.2161

[49] Zhou XD, Chen ZP (2015) Preparation and performance evaluation of emulsomes as a drug delivery system for silybin. Arch Pharm Res 38(12):2193–2200. doi:10.1007/s12272-015-0630-7

[50] Xie YC, Yi YN, Hu XW, Shangguan M, Wang LJ, Lu Y, Qi JP, Wu W (2016) Synchronous microencapsulation of multiple components in silymarin into PLGA nanoparticles by an emulsification/solvent evaporation method. Pharm Dev Technol 21(6):672–679. doi:10.3109/10837450.2015.1045616

[51] Cigu TA, Vasiliu S, Racovita S, Lionte C, Sunel V, Popa M, Cheptea C (2016) Adsorption and release studies of new cephalosporin from chitosan-g-poly(glycidyl methacrylate) microparticles. Eur Polym J 82:132–152. doi:10.1016/j.eurpolymj.2016.07.011

[52] Jia H, Kerr LL (2015) Kinetics of drug release from drug carrier of polymer/TiO_2 nanotubes composite—pH dependent study. J Appl Polym Sci. doi:10.1002/app.41570

[53] Bravo SA, Lamas MC, Salomón CJ (2002) In-vitro studies of diclofenac sodium controlled-release from biopolymeric hydrophilic matrices. J Pharm Pharm Sci 5(3):213–219

[54] Dash S, Murthy PN, Nath L, Chowdhury P (2010) Acta Pol Pharm 67(3):217–223

[55] Xu S, Yin BR, Guo J, Wang CC (2013) Biocompatible hollow magnetic supraparticles: ultrafast microwave-assisted synthesis, casein-micelle-mediated cavity formation and controlled drug delivery. J Mater Chem B 1(33):4079–4087. doi:10.1039/c3tb20238k

[56] Huang SJ, Ke JH, Chen GJ, Wang LF (2013) One-pot synthesis of PDMAEMA-bound iron oxide nanoparticles for magnetofection. J Mater Chem B 1(43):5916–5924. doi:10.1039/c3tb21149e

[57] Efthimiadou EK, Tapeinos C, Chatzipavlidis A, Boukos N, Fragogeorgi E, Palamaris L, Loudos G, Kordas G (2014) Dynamic in vivo imaging of dual-triggered microspheres for sustained release applications: synthesis, characterization and cytotoxicity study. Int J Pharm 461(1–2):54–63. doi:10.1016/j.ijpharm.2013.11.03